Chemical Science

ROYAL SOCIETY OF CHEMISTRY

EDGE ARTICLE

View Article Online
View Journal | View Issue

Cite this: *Chem. Sci.*, 2025, **16**, 18806

All publication charges for this article have been paid for by the Royal Society of Chemistry

Single-molecule graphene quantum dots: enhancement of optical properties and promotion of photodynamic efficacy based on precise control of the electronic structure

Jintao Chen,[a] Bin Li,[a] Daoyuan Liu,[a] Shiru Yin,[a] Ji Qi,[a] Zhenming Lu,*[a] Yi Liu *[ab] and Tian Gao *[a]

Graphene quantum dots (GQDs) exhibit excellent optical properties, low toxicity, good biocompatibility, and high re-active oxygen species (ROS) generation efficiency under photoexcitation, demonstrating significant potential for achieving visualized therapy. However, conventional synthesis methods yield GQDs as multi-component mixtures with compromised safety and consistency, coupled with unclear luminescence mechanisms and difficulties in precise microstructure control, which severely hinder their development as nanomedicines. Therefore, it is urgent to synthesize mono-component single-molecule GQDs and systematically investigate the structure–property relationships governing their optical characteristics and ROS generation capabilities. This work established a modular organic synthetic strategy based on electron donor–acceptor (D–A) architectures, successfully preparing three single-molecule GQDs with identical core structures but distinct edge functionalization: 12Me-GQD (12D–A), 12Br-GQD (D–12A), and 6Br-6Me-GQD (6D–π–6A). Systematic characterization reveals that electron-donating groups ($-CH_3$) induce a blue shift in photoluminescence (PL) emission, enhance fluorescence quantum yield, and improve photo-induced ROS production. Conversely, electron-withdrawing groups (–Br) cause emission red shift, reduce PL quantum yield, and completely suppress photodynamic activity. Notably, the alternately substituted 6Br-6Me-GQD exhibits enriched electron transfer pathways, demonstrating dual emission peaks and optimal photodynamic performance. Importantly, both 12D–A type and 6D–π–6A type GQDs maintain effective ROS generation under hypoxic conditions, addressing the critical limitation of conventional photosensitizers in oxygen-deprived tumor microenvironments. This work established a modular synthetic system for single-molecule GQDs with different D–A types and revealed the structure–property relationships governing optical characteristics and ROS generation capabilities, providing novel insights for the development of hypoxia-adaptive PDT nanomedicine.

Received 18th May 2025
Accepted 8th September 2025

DOI: 10.1039/d5sc03593g

rsc.li/chemical-science

Introduction

Graphene quantum dots (GQDs) have been extensively investigated for biomedical applications due to their unique optical properties, favorable biosafety, and exceptional photosensitivity, demonstrating significant potential as novel "theranostic" nanomedicines integrating diagnosis and therapy.[1–3] For instance, Yan *et al.* successfully engineered a PEG-modified GQD system that enables multimodal tumor imaging through fluorescence, photoacoustic (PA), and magnetic resonance imaging (MRI).[4] Hassnain *et al.* designed carboxyl-functionalized cGQDs with high singlet oxygen ($^1O_2$) quantum yields, demonstrating remarkable antibacterial efficacy by suppressing over 99.9% of drug-resistant *Staphylococcus aureus* and *Escherichia coli*.[5] Kuo *et al.* created amino-functionalized two-photon photosensitizers (amino-N-GQDs) that emit intense green fluorescence in tumor cells and effectively inhibit multidrug-resistant cancer cells through photodynamic therapy (PDT).[6]

However, the pharmaceutical development of GQDs is confronted with three major challenges. First, GQDs synthesized *via* conventional methods exist as multicomponent mixtures, where structural homogeneity and batch-to-batch variability critically constrain their applications as nanomedicines.[7] For instance, GQDs prepared through exfoliation of graphite or

[a]*School of Chemistry and Chemical Engineering, Interdisciplinary Institute of NMR and Molecular Sciences, Hubei Province Key Laboratory for Coal Conversion and New Carbon Materials, Institute of Advanced Materials and Nanotechnology, Wuhan University of Science and Technology, Wuhan 430081, P. R. China. E-mail: gaotian@whu.edu.cn; luzhenming@wust.edu.cn*

[b]*Key Laboratory of Catalysis and Energy Materials Chemistry of Ministry of Education, Hubei Key Laboratory of Catalysis and Materials Science, School of Chemistry and Materials Science & School of Pharmaceutical Sciences, South-Central Minzu University, Wuhan 430074, P. R. China. E-mail: yiliuchem@whu.edu.cn*

carbon fibers, or high-temperature/high-pressure carbonization of small molecules, exhibit inherent limitations in precise control over core conjugation area, surface functional group types/quantities, and material layer numbers. These inconsistencies fail to meet the strict drug consistency requirements mandated by regulatory authorities.[8,9] Additionally, the structural heterogeneity complicates the differentiation between bioactive components and potential toxic elements, rendering biosafety assurance problematic. Consequently, the development of novel synthetic systems capable of efficiently producing monodisperse single-molecule GQDs is urgently required to advance biomedical applications.[10–12]

The optical properties of GQDs are pivotal for bioimaging and biodetection, yet their emission mechanisms remain contentious, hindering rational design and optimization of optical performance.[13] Conventional strategies for tuning GQD luminescence primarily involve size modulation, surface oxidation control, and edge functionalization. For example, Cao *et al.* proposed that fluorescence variations of MCDs are affected by their size and graphitic nitrogen content. Increased MCD size correlates with elevated graphitic nitrogen levels, resulting in reduced energy gaps and red-shifted emission wavelengths.[14] Sk *et al.* employed density functional theory (DFT) and time-dependent DFT to simulate photoluminescence behavior of GQDs, revealing that size, shape, edge configurations, chemical substituents, heteroatom doping, and surface defects collectively govern emission properties.[15] Meanwhile, Dang *et al.* established an atomic-level identification framework for oxygen functional groups through thermal stability and electronic analyses, uncovering dynamic evolution patterns of oxygen species on carbon surfaces.[16] Although these studies advance our understanding of GQD property regulation, the intricate microstructure of GQDs still prevents researchers from systematically quantifying precise structure–property relationships between atomic configurations and luminescence. Therefore, fabricating GQDs with uniform core architectures and tunable surface functionalities under single-variable control is essential to elucidate emission mechanisms through systematic structure–property correlation studies.

GQDs exhibit outstanding performance in PDT for antitumor applications, owing to their superior photosensitivity and ability to generate abundant reactive oxygen species (ROS) upon light excitation, with singlet oxygen quantum yields exceeding 80%, significantly surpassing the efficiency of commercial photosensitizers.[17] For instance, Ge *et al.* synthesized GQDs from polythiophene precursors *via* a hydrothermal method in alkaline solutions, demonstrating highly efficient singlet oxygen generation under irradiation.[17] Tan *et al.* developed GQDs with dual photodynamic and photothermal functionalities, achieving remarkable antitumor efficacy in murine models.[18] Yang *et al.* designed acidity-activated GQDs for prolonged tumor imaging and sustained PDT applications.[19] However, the intricate microstructure of GQDs obscures the mechanism of light-induced ROS generation, hindering in-depth exploration of the structure–activity relationships governing their PDT efficacy. In contrast, small-molecule photosensitizers are typically designed based on electron donor–acceptor (D–A) structures, where PDT mechanisms are well-defined.[20] Their molecular structures can be strategically optimized by modulating donor/acceptor moieties or electron transfer pathways to enhance PDT performance.[21,22] Yet, conventional methods fail to precisely engineer D–A configurations in GQDs, leaving the influence of electronic structures on photosensitizing effects unexplored. Consequently, synthesizing monodisperse single-molecule GQDs with tailored D–A architectures is critical for elucidating the structure–activity relationships between electronic configurations and PDT outcomes, as well as for revealing ROS generation mechanisms.

This work establishes a modular synthesis system for single-molecule GQDs through a series of organic reactions, enabling precise donor–acceptor (D–A) structural engineering. Three distinct D–A type GQDs with identical core architectures but varied edge functionalities were synthesized: 12D–A type (12Me-GQD, only methyl-substituted), D-12A type (12Br-GQD, only bromine-substituted), and 6D–π–6A type (6Br-6Me-GQD, alternating bromine/methyl substitution). This approach achieves atomic-level control over the substituent type (electron-donating $-CH_3$ *vs.* electron-withdrawing -Br), quantity, and spatial distribution (single kind of group substitution *vs.* alternating patterns). Using controlled-variable methodologies combined with spectroscopic and energy spectrum analyses, we systematically investigated how D–A configurations modulate band structures and optical properties-including fluorescence emission wavelength, quantum yield, and lifetime, thereby elucidating fundamental structure–property relationships. Furthermore, fluorescence spectroscopy, UV-vis absorption spectroscopy, and ultraviolet photoelectron spectroscopy (UPS) were employed to quantify ROS generation under hypoxic conditions and correlate PDT efficacy with D–A architectures, revealing critical structure–activity dependencies. This work pioneers a modular synthesis system for single-molecule GQDs, advancing the study of edge functionalization effects on electronic structures, luminescence behaviors, and PDT efficiency. By transitioning from conventional ensemble-averaged analyses to atomically precise, single-variable-controlled investigations, it provides unprecedented insights into structure–performance correlations of GQDs. This work not only deepens the mechanistic understanding of GQD photo-physics but also establishes a foundational framework for developing single-molecule nanomedicines with tailored functionalities.

Results and discussion

Modular synthesis and electronic structure modulation of single-molecule GQDs

Modular synthesis system for single-molecule GQDs. Conventional GQDs preparation methods fail to produce monodisperse nanomaterials. Top-down fragmentation or bottom-up high-pressure polymerization of organic precursors inevitably yields structurally heterogeneous mixtures. Moreover, sp^2-conjugated regions in synthetically derived polycyclic graphene molecules readily undergo π–π stacking-induced aggregation, hindering further structural refinement. To address these limitations, this work develops a "modular

assembly-directed aromatization" strategy that integrates functional groups during the molecular coupling stage to sterically suppress π–π stacking. As illustrated in Fig. 1A, this three-stage modular synthesis, comprising "organic precursor coupling", "polycyclic conjugation", and "dehydrogenative planar aromatization", enables atomic-level precision in fabricating structurally uniform single-molecule GQDs. Stage 1: Organic precursor coupling. Starting with 3′-bromoacetophenone, intermediate 1 was synthesized *via* self-condensation (87% yield).

Subsequent site-specific Sonogashira coupling introduced alkynyl groups, yielding key intermediate 2 (86% yield; Fig. S1). Parallelly, 4′-R-phenylacetic acids (R = Me, Br) were decarboxylated under DCC/4-DMAP catalysis to generate *para*-disubstituted intermediates 3–*X* (3–1, 3–2), which underwent condensation–cyclization to form cyclopentadienone intermediates 4–*X* (4–1, 4–2, 4–3) with tailored edge functionalities (66%, 83%, and 95% yields, respectively; Fig. S2–S4). Stage 2: Polycyclic assembly. Diels–Alder cycloaddition between intermediates 2 and 4–*X* produced polycyclic aromatic hydrocarbons

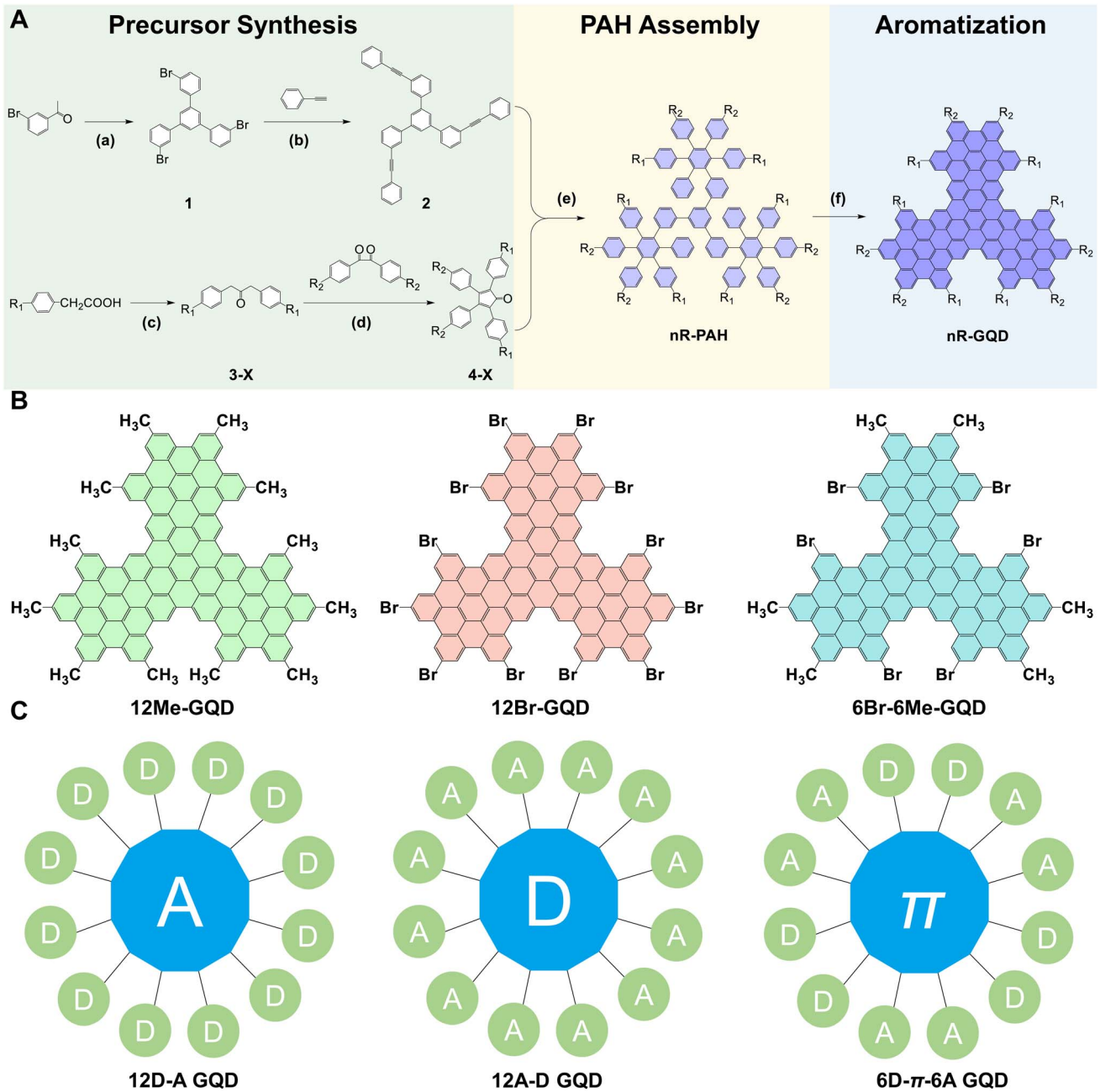

Fig. 1 Modular synthesis of single-molecule GQDs. (A) (a) $SOCl_2$, EtOH, 80 °C, 1 h, yield: 87%. (b) Pd $(PPh_3)_2Cl_2$/CuI, Toluene/Et_3N, N_2, 100 °C, 24 h, yield: 86%. (c) DCC/4-DMAP, DCM, Ar, rt, 24 h, yield: 78–88%. (d) KOH/EtOH, 70 °C, 1 h, yield: 66–95%. (e) Ph_2O, 250 °C, 10 h, yield: 37–40%. (f) $FeCl_3$, CH_3NO_2, DCM, rt, 2 h, yield: 46–60%. R_1: Me, Br. R_2: Me, Br. (B) Three single-molecule GQDs. (C) Schematic representation of the structure of three single-molecule GQDs. D: electron donor; A: electron acceptor.

(PAHs) with precisely engineered edge substituents: 12Me-PAH, 12Br-PAH, and 6Br-6Me-PAH. Stage 3: Dehydrogenative planar aromatization. Scholl oxidation of PAHs using $FeCl_3$ in DCM/CH_3NO_2 facilitated planar fusion, yielding single-layer conjugated GQDs (12Me-GQD, 12Br-GQD, and 6Br-6Me-GQD) with yields of 60%, 55%, and 46%, respectively (Fig. S5–S7). All intermediates were structurally validated by using ^{1}H NMR, ^{13}C NMR and MS spectra (Fig. S8–S37).

The "three-stage modular" synthesis system for single-molecule GQDs enables rapid and precise edge functionalization, outperforming conventional methods. By simply varying substituents on monocyclic precursors (*e.g.*, 4′-R-phenylacetic acid) while maintaining identical reaction types and conditions in subsequent steps, this approach significantly reduces the complexity of post-synthetic functional group engineering. In contrast, unfunctionalized polycyclic aromatic hydrocarbons (PAHs) or graphene derivatives are prone to π–π stacking-induced aggregation, forming precipitated macroparticles that hinder further precise functionalization. This strategy circumvents such limitations by pre-installing substituents at the molecular precursor stage, leveraging steric hindrance to suppress PAH aggregation during synthesis. The resulting single-molecule GQDs (*e.g.*, 12Me-GQD, 12Br-GQD, and 6Br-6Me-GQD) exhibit long-term colloidal stability in solvents such as $CHCl_3$. Furthermore, the modular framework allows functional diversification by substituting precursors with tailored moieties (*e.g.*, $-NH_2$ and –COOH derivatives), thereby enabling the integration of multifunctional capabilities into single-molecule nanomaterials.

Electronic structure modulation of single-molecule GQDs. As illustrated in Fig. 1B, the three single-molecule GQDs, 12Me-GQD, 12Br-GQD, and 6Br-6Me-GQD, possess identical core structures composed of 132 sp^2-conjugated carbon atoms arranged in planar armchair-edged configurations, with uniform edge functionalization (12 groups at identical positions), enabling controlled-variable studies on substituent-dependent electronic properties. Their divergent edge functionalities, 12 electron-donating methyl ($-CH_3$) groups in 12Me-GQD, 12 electron-withdrawing bromine (–Br) substituents in 12Br-GQD, and an alternating pattern of six -Br and six $-CH_3$ groups in 6Br-6Me-GQD, directly modulate molecular electronic architectures, yielding distinct donor–acceptor (D–A) configurations: a 12D–A type structure (uniform donor periphery), a D–12A type structure (uniform acceptor periphery), and a 6D–π–6A type hybrid (alternating donor/acceptor alignment), respectively (Fig. 1C). Notably, the sp^2-conjugated carbon cores exhibit adaptable electronic roles, functioning as electron acceptors, donors, or π-bridges, depending on the electronic polarization of edge substituents, highlighting the versatility of carbon nanomaterials in achieving programmable electronic structures through rational edge engineering (Fig. S38). This structural uniformity in core geometry and edge positioning, combined with precise substituent control, establishes a foundational platform for elucidating structure–property relationships in nanoscale carbon systems.

Morphology and molecular weight

Morphology, size, thickness, and lattice analysis of single-molecule GQDs. As shown in Fig. 2A–C, all three single-molecule GQDs (12Me-GQD, 12Br-GQD, and 6Br-6Me-GQD) exhibit nanoscale dimensions and monodisperse circular morphologies. Their average particle diameters, measured to be 3.08 ± 0.08 nm (12Me-GQD), 6.00 ± 0.00 nm (12Br-GQD), and 3.32 ± 0.02 nm (6Br-6Me-GQD), align well with theoretical values derived from molecular structures. Particle size distributions follow Gaussian profiles (insets of Fig. 2A–C), with coefficients of determination (R^2) exceeding 0.97. Notably, the significant increase in particle diameter ($\Delta d_{avg} = 2.92$ nm) for 12Br-GQD compared to 12Me-GQD arises from the larger atomic radius of bromine substituents, which induces steric and electronic effects (Fig. S38), stabilizing larger conformations during solvent evaporation. High-resolution TEM (HRTEM) images (insets of Fig. 2A–C) reveal distinct lattice fringes with a spacing of 0.24 nm, corresponding to the (100) crystallographic plane of graphite, confirming the integrity of the sp^2-conjugated carbon cores in all three GQDs. This observation validates the preservation of planar aromatic frameworks despite edge functionalization, underscoring the structural precision of the modular synthesis strategy.

Atomic force microscopy (AFM) images (Fig. 2D–F) confirm the monodisperse nature of all three single-molecule GQDs, with average thicknesses of 0.83 nm (12Me-GQD), 0.82 nm (12Br-GQD), and 0.83 nm (6Br-6Me-GQD), consistent with monolayer characteristics. The three-dimensional height profiles (insets of Fig. 2D–F) further verify their planar single-layer structures, demonstrating that edge functionalization with methyl or bromine groups does not significantly alter molecular thickness.

Precise molecular weight determination and structural validation were performed *via* matrix-assisted laser desorption/ionization time-of-flight mass spectrometry (MALDI-TOF-MS). As shown in Fig. 2G–I, the measured molecular weights of 12Me-GQD ($C_{144}H_{66}$, *m*/*z* 1796.11), 12Br-GQD ($C_{132}H_{30}Br_{12}$, *m*/*z* 2574.54), and 6Br-6Me-GQD ($C_{138}H_{48}Br_6$, *m*/*z* 2185.33) closely match theoretical values (Table S1). The exclusive presence of single peaks in all MALDI-TOF spectra, with no dimeric or polymeric species detected, confirms the successful synthesis of monodisperse, structurally uniform nanomaterials through this modular strategy.

Micro structure

Crystallographic diffraction analysis. Fig. 3A displays the powder X-ray diffraction (XRD) patterns of the three single-molecule GQDs, all exhibiting characteristic short-range ordered features. The diffraction peaks observed at approximately 25°, 31°, 43°, and 56° correspond to the (002), (110), (103), and (004) crystallographic planes of graphite, respectively.

The XRD data further reveal the stacking configuration of carbon-based nanomaterials. By applying the Bragg equation ($n\lambda = 2d\sin\theta$) to the (002) diffraction angle, the interlayer spacings (d_{002}) were calculated to be 3.74 Å (12Me-GQD), 3.68 Å

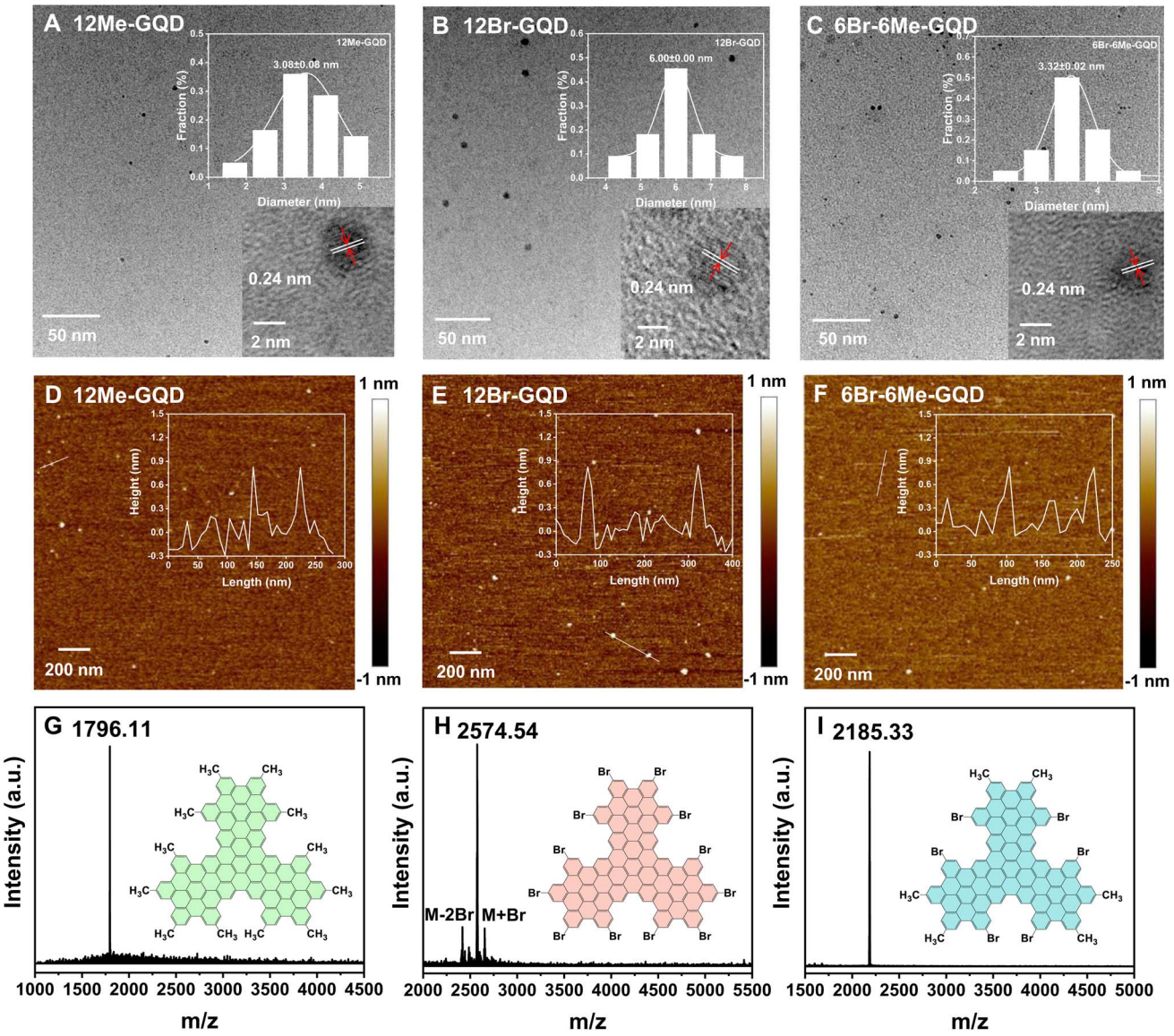

Fig. 2 (A) HRTEM image of 12Me-GQD. (B) HRTEM image of 12Br-GQD. (C) HRTEM image of 6Br-6Me-GQD (top-right inset shows statistical size distribution and Gaussian curve fitting; bottom-right inset shows lattice fringes). (D) AFM image of single-molecule 12Me-GQD. (E) AFM image of 12Br-GQD. (F) AFM image of 6Br-6Me-GQD (bottom right inset shows the height change at the marker line). (G) MALDI-TOF-MS of 12Me-GQD. (H) MALDI-TOF-MS of 12Br-GQD. (I) MALDI-TOF-MS of 6Br-6Me-GQD.

(12Br-GQD), and 3.50 Å (6Br-6Me-GQD).[23] Notably, these values significantly exceed the standard graphite interlayer spacing (3.35 Å), indicating that steric hindrance effects from edge functional groups (–CH_3/–Br) restrict intermolecular π–π stacking, resulting in loosely packed layered structures. The slightly smaller interlayer spacing of 12Br-GQD compared to 12Me-GQD ($\Delta d = 0.06$ Å) arises from dipole–dipole interactions induced by the higher electronegativity of Br atoms, which influence molecular bending and mitigate structural distortion (Table S2).

Raman spectroscopic analysis. Raman spectra of graphite and graphitic materials typically exhibit characteristic D, G, 2D, and other bands, where peak positions and intensity ratios (*e.g.*, I_D/I_G) provide critical insights into conjugation extent, defect density, layer number, and interlayer interactions.[24] As shown in Fig. 3B, under 532 nm laser excitation, the Raman spectra of the three single-molecule GQDs display hallmark carbonaceous peaks: D band (1350 cm^{-1}), G band (1590 cm^{-1}), 2D band (2720 cm^{-1}), D + G band (2900 cm^{-1}), and 2D′ band (3120 cm^{-1}). Notably, the I_D/I_G ratio aligns closely with reported values for nano-graphene, indicating a defect-free, short-range ordered sp^2-conjugated core structure, consistent with HRTEM lattice observations. Importantly, the D-band intensity arises from intrinsic phonon scattering enhancement caused by armchair-edge configurations at the GQD periphery, rather than structural defects. The single Lorentzian line shapes of the 2D, D + G, and 2D′ bands confirm a strictly monolayer architecture with negligible interlayer coupling. Further analysis (Fig. 3C–E and Table S3) reveals that variations in Raman parameters (*e.g.*, I_D/I_G and peak positions) among the three GQDs are <6%,

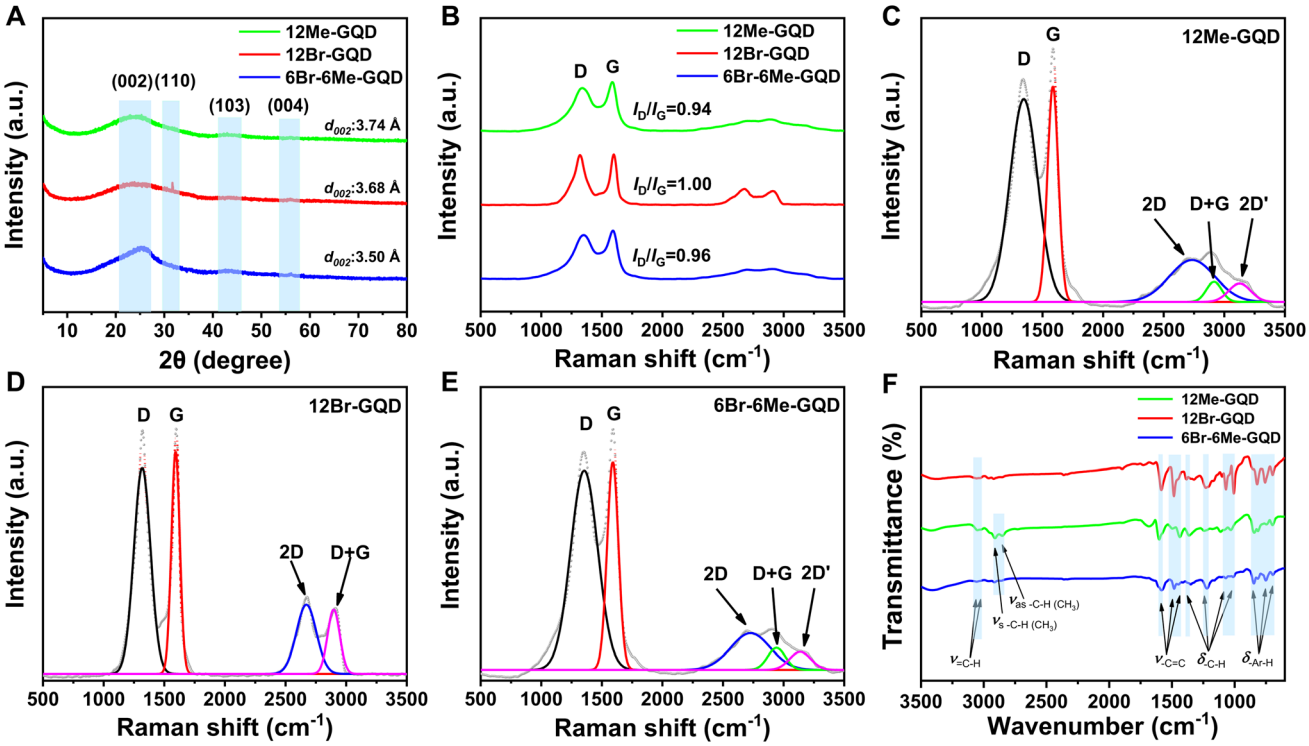

Fig. 3 (A) Powder XRD spectra of 12Me-GQD, 12Br-GQD and 6Br-6Me-GQD. (B) Raman spectra of 12Me-GQD, 12Br-GQD and 6Br-6Me-GQD. (C) Raman spectral peak fitting of 12Me-GQD. (D) Raman spectral peak fitting of 12Br-GQD. (E) Raman spectral peak fitting of 6Br-6Me-GQD. (F) FTIR spectra of 12Me-GQD, 12Br-GQD and 6Br-6Me-GQD.

demonstrating that edge substituents (–CH_3/–Br) do not disrupt the sp^2 conjugation framework's electron-phonon coupling. This validates the modular synthesis strategy for achieving precise edge functionalization while preserving core structural integrity.[25]

Thermal stability analysis. Thermogravimetric analysis (TGA) directly probes the structural integrity and thermal robustness of carbon nanomaterials.[26] As shown in Fig. S39, prior to Scholl dehydrogenation, Br-containing PAH precursors exhibited significant mass loss (Δm > 10%) at 200 °C. In contrast, all three single-molecule GQDs retained over 80% mass at 450 °C after cyclization, confirming that the Scholl reaction successfully constructs a rigid, thermally stable sp^2-conjugated core. At elevated temperatures (450–600 °C), mass decline in GQDs arises from gradual pyrolysis and graphitic reorganization of the carbon framework, consistent with reported nanographene behavior. Thermal stability variations among the GQDs correlate with their functional groups. 12Me-GQD exhibited the highest residual mass (72.64% at 900 °C), attributed to the electron-donating effect of –CH_3 groups, which stabilize the carbon skeleton *via* σ–π hyperconjugation. Conversely, 12Br-GQD showed the lowest residual mass (59.96% at 900 °C) due to C–Br bond cleavage (releasing HBr above 600 °C) and electron-withdrawing effects of Br, which reduce resonance stabilization. 6Br–6Me-GQD displayed intermediate stability, suggesting mutual cancellation of electronic effects between alternating –CH_3 and –Br groups. Notably, pre-decomposition mass losses (Δm > 10% at 200 °C) observed in 12Br-PAH and 6Br-6Me-PAH (absent in 12Me-PAH) reflect edge Br degradation, further highlighting the thermal stability advantage of –CH_3 substitution. Collectively, TGA data validate the high structural integrity of single-molecule GQDs, elucidate substituent-dependent degradation mechanisms, and provide critical parameters for high-temperature applications (*e.g.*, catalytic supports and thermal-resistant coatings).

Surface structure

Fourier transform infrared (FTIR) spectroscopy characterization. Fig. S40A and 3F present the FTIR spectra of three single-molecule GQDs and their corresponding PAH precursors, respectively. Fig. S40B–D provide detailed comparisons of the PAH precursors before and after the Scholl reaction, elucidating the molecular mechanism of chemical bond evolution during the planar fused cyclization process. As summarized in Table S4, in the C–H stretching vibration region (2800–3100 cm^{-1}) characteristic of sp^2-conjugated frameworks, the single-molecule GQDs exhibit two distinct peaks at 3054 cm^{-1} and 3023 cm^{-1}, corresponding to asymmetric (ν_{as}) and symmetric (ν_s) stretching modes of sp^2-hybridized aromatic C–H bonds. In the C=C skeletal vibration region (1400–1600 cm^{-1}), the intensity of characteristic peaks at 1583 cm^{-1} ($\nu_{C=C}$), 1498 cm^{-1} (ring breathing vibration), and 1439 cm^{-1} (C–C in-plane stretching) is markedly enhanced, confirming the formation of extended sp^2-conjugated domains *via* intramolecular dehydrogenation during the Scholl reaction. In the C–H in-plane deformation region (1200–1000 cm^{-1}), the strong absorption

peaks of PAH precursors at 1220 cm^{-1} (δ_{C-H}, in-plane bending), 1068 cm^{-1} (coupled ring deformation), and 1007 cm^{-1} (C–C stretching) show 60–75% intensity reduction in GQDs, directly reflecting the elimination of pendant C–H bonds on phenyl groups through cyclization, yielding a coplanar sp^2-conjugated molecular architecture. In the C–H out-of-plane bending region (600–900 cm^{-1}), characteristic peaks of PAHs at 821 cm^{-1} (*ortho*-disubstituted), 757 cm^{-1} (meta-substituted), and 696 cm^{-1} (monosubstituted) nearly vanish in GQDs. These observations indicate the efficient cleavage of isolated C–H bonds *via* Scholl reaction-driven dehydrogenation, demonstrating the high efficacy of fused cyclization in constructing single-molecule GQDs.[27]

Distinct infrared spectral features were observed among the three single-molecule GQDs. For 12Me-GQD and 6Br-6Me-GQD, characteristic asymmetric ($\nu_{as\ C-H}$, 2910 cm^{-1}) and symmetric ($\nu_{s\ C-H}$, 2854 cm^{-1}) stretching vibrations of methyl groups were identified, with an intensity ratio ($I_{2910}/I_{2854} = 1.3$) consistent with typical methyl vibrational modes, confirming successful edge $-CH_3$ functionalization. In contrast, 12Br-GQD and 6Br-6Me-GQD exhibited broadened absorption bands in the 600–800 cm^{-1} region, attributed to C–Br bending vibrations (δ_{C-Br}, ~650 cm^{-1}) coupled with Br–π interactions. The weak signal intensity in this region suggests that bromine atoms predominantly influence the optical properties of GQDs through electronic effects rather than vibrational modes.

X-ray photoelectron spectroscopy (XPS) characterization. The full XPS spectra of the three single-molecule GQDs (Fig. S41A, C, and F) confirm their elemental compositions, consistent with their molecular structures. 12Me-GQD exhibits only carbon signals (C 1s: 284.0 eV), while 12Br-GQD and 6Br-6Me-GQD display both carbon (C 1s) and bromine (Br 3d) signals, demonstrating the precision of the modular synthesis strategy in tailoring edge functionalities. High-resolution C 1s spectra (Fig. S41B, D and G) reveal shared sp^2-conjugated carbon cores (dominant peak at 284.0 eV) but distinct edge bonding patterns. For 12Me-GQD, a weak peak at 284.4 eV corresponds to sp^3-hybridized C–C bonds from edge methyl groups. In 12Br-GQD, the characteristic peak at 284.8 eV arises from C–Br bonds, with intensity proportional to the theoretical bromine content (12 Br/GQD). The higher sp^3-carbon ratio in 6Br-6Me-GQD reflects synergistic modulation of edge chemistry by alternating substituents. All samples exhibit π–π* satellite peaks near 290 eV, confirming quantum confinement effects within the conjugated cores. Br 3d high-resolution spectra (Fig. S41E and H) for 12Br-GQD and 6Br-6Me-GQD show doublet splitting (C–Br $3d_{5/2}$: 69.7 eV; C–Br $3d_{3/2}$: 70.7 eV) with a spin–orbit splitting energy of 1.0 eV, characteristic of covalent C–Br bonds and excluding Br_2 (68 eV) or Br^- (67 eV) impurities. These results validate the modular synthesis strategy, which achieves atomic-level control over edge functionalization while preserving the structural integrity of the sp^2-conjugated cores.[28]

Optical properties and the energy band structure

Fluorescence emission properties and analysis. Fig. 4A–C present the fluorescence emission spectra of the three single-molecule GQDs, revealing excitation-independent emission behavior, where emission wavelengths remain constant across varying excitation wavelengths, a hallmark of molecular-state luminescence distinct from conventional multicomponent GQDs.[29] Specifically, 12Me-GQD exhibits a dominant emission peak at 502 nm (FWHM = 130 nm) with shoulder peaks at 442 nm and 644 nm. Similarly, 12Br-GQD displays a primary peak at 621 nm (FWHM = 114 nm) accompanied by a shoulder at 558 nm. These secondary peaks arise from core-edge state coupling, where π–π* transitions in the sp^2-conjugated core interact with charge-transfer states localized at edge functional groups ($-CH_3$/–Br). Notably, 6Br-6Me-GQD demonstrates dual emission peaks at 409 nm and 476 nm (Table S5), indicative of multiple excited-state energy levels induced by its alternating substituent architecture. A comparative analysis highlights a significant redshift ($\Delta\lambda = 119$ nm) in the primary emission of 12Br-GQD relative to 12Me-GQD, underscoring the profound influence of edge functionalities on luminescence. The strong electron-withdrawing effect of bromine (Hammett constant $\sigma_p = +0.23$) lowers the LUMO energy level, reducing the bandgap to 4.00 eV, whereas the electron-donating methyl groups ($\sigma_p = -0.17$) in 12Me-GQD increase the bandgap to 4.17 eV (Fig. S44). This demonstrates that the electron-donating/withdrawing capacity of edge groups directly modulates energy level structures, enabling precise tuning of fluorescence spectra and apparent emission colors. The distinct emission colors of the three GQDs are evident in CIE chromaticity coordinates (Fig. 4I and S42). Under 365 nm excitation, 12Me-GQD, 12Br-GQD, and 6Br-6Me-GQD emit blue (0.25, 0.34), red (0.55, 0.43), and green (0.17, 0.25) fluorescence, respectively, spanning the entire visible spectrum. This full-color tunability expands their utility in multicolor imaging and fluorescence labeling while highlighting potential for RGB (red-green-blue) optical device integration.[30]

Fluorescence lifetimes and quantum yields. Time-resolved fluorescence spectroscopy, critical for elucidating excited-state dynamics,[31,32] revealed distinct fluorescence lifetimes for the three single-molecule GQDs: 9.26 ns (12Me-GQD), 4.10 ns (12Br-GQD), and 3.62 ns (6Br-6Me-GQD) (Fig. 4D–F). Exponential decay analysis (Table S6) showed that 12Me-GQD follows a bi-exponential decay ($\tau_1 = 3.84$ ns, $\tau_2 = 12.65$ ns, $R_1 : R_2 = 0.6 : 1$), indicative of competing radiative pathways involving core π–π* transitions and edge-to-core charge recombination. In contrast, 12Br-GQD exhibits a triexponential decay ($\tau_1 = 0.84$ ns, $\tau_2 = 2.89$ ns, $\tau_3 = 6.84$ ns), attributed to spin–orbit coupling (SOC) enhancement by bromine atoms, which activates triplet-state participation. Meanwhile, 6Br-6Me-GQD displays a bi-exponential decay ($\tau_1 = 1.39$ ns, $\tau_2 = 6.15$ ns, $R_1 : R_2 = 1.1 : 1$), reflecting synergistic modulation of excited-state lifetimes by alternating donor–acceptor substituents. Absolute photoluminescence quantum yields (PLQY) further differ significantly: 9.15% (12Me-GQD), 5.53% (6Br-6Me-GQD), and 4.22% (12Br-GQD) (Fig. S43). This trend correlates with substituent electronic properties: methyl groups ($-CH_3$) enhance σ–π hyperconjugation, stabilizing singlet excited states and suppressing nonradiative decay (k_{nr}), thereby improving QY. Conversely, bromine substituents induce heavy-atom effects,

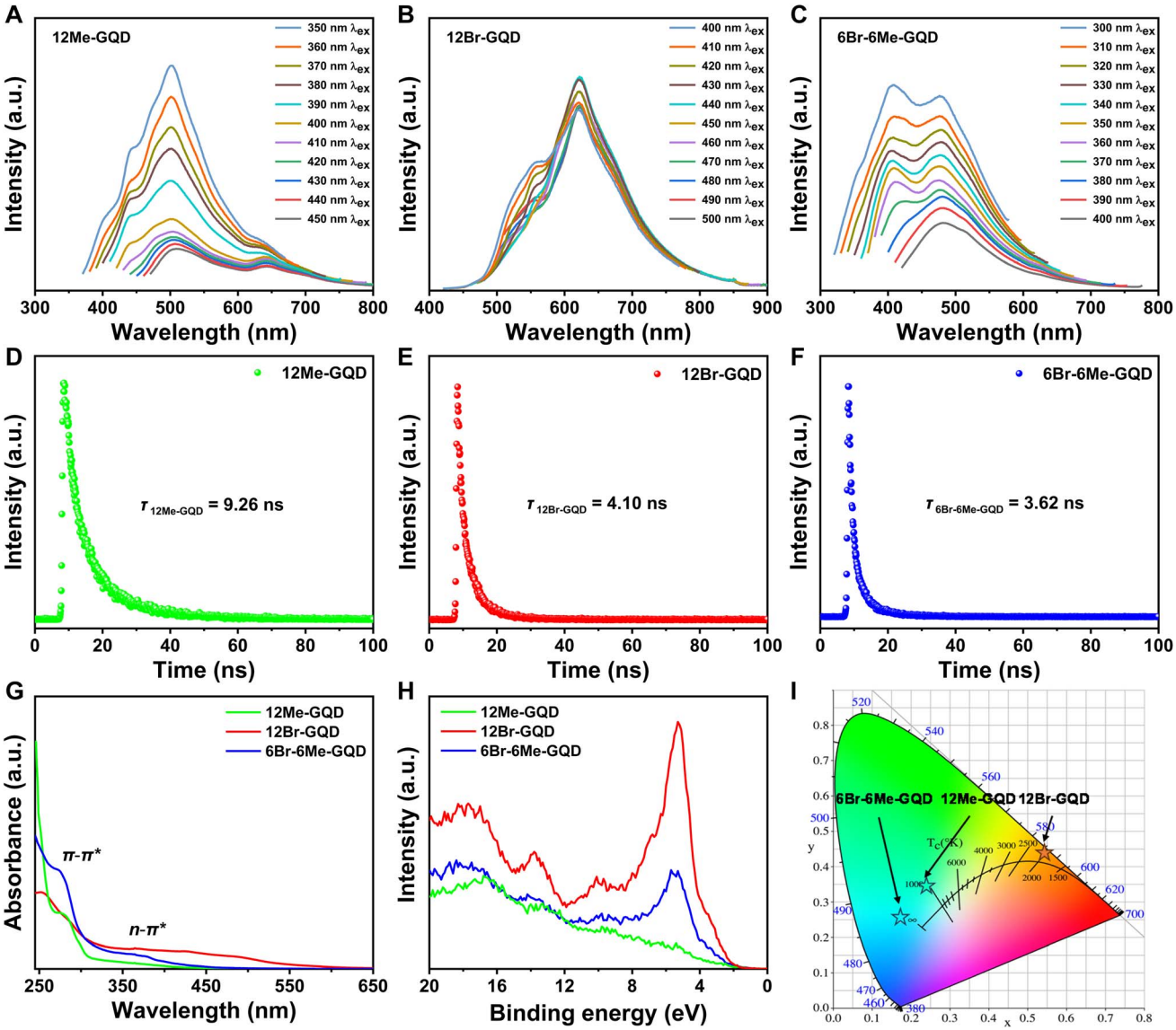

Fig. 4 (A) FL emission spectrum of 12Me-GQD. (B) FL emission spectrum of 12Br-GQD. (C) FL emission spectrum of 6Br-6Me-GQD. (D) PL decay curves of 12Me-GQD. (E) PL decay curves of 12Br-GQD. (F) PL decay curves of 6Br-6Me-GQD. (G) UV-vis absorption spectra of 12Me-GQD, 12Br-GQD and 6Br-6Me-GQD. (H) Valence band X-ray spectra of 12Me-GQD, 12Br-GQD and 6Br-6Me-GQD. (I) CIE color coordinates of 12Me-GQD, 12Br-GQD and 6Br-6Me-GQD.

accelerating intersystem crossing (k_{ISC}) to nonradiative triplet states and reducing QY. These findings underscore the critical role of edge functionalization in governing both excited-state kinetics and luminescence efficiency, providing a mechanistic basis for rational design of single-molecule GQDs with tailored optoelectronic performance.

UV-vis absorption spectroscopy and bandgap engineering. As shown in Fig. 4G and Table S7, the UV-vis absorption spectra of the three single-molecule GQDs exhibit intense peaks near 270 nm, corresponding to π–π* transitions within the sp^2-conjugated carbon cores, and broad absorption bands between 300 and 500 nm, attributed to *n*–π* charge transfer from edge functional groups (C–Br/C–Me → sp^2 core).[33] For 12Me-GQD, the electron-donating methyl (–CH_3) groups extend the conjugation through σ–π hyperconjugation, blue-shifting the n–π* absorption peak to 297 nm and increasing the optical bandgap. Conversely, the electron-withdrawing bromine substituents in 12Br-GQD and 6Br-6Me-GQD induce red-shifted n–π* transitions. Further analysis of the Tauc plots (Fig. S44) reveals bandgap energies (E_g) of 4.00–4.18 eV for these GQDs, significantly higher than that of conventional GQDs (E_g = 2–3 eV). This enhancement arises from molecular-scale quantum confinement effects (size < exciton Bohr radius) and the defect-free sp^2-conjugated core architecture, which collectively suppress charge carrier delocalization and elevate energy levels. These findings demonstrate precise bandgap modulation through edge functionalization, advancing the rational design of GQDs for tailored optoelectronic applications.[34]

Valence band structure and Fermi level modulation. Valence band X-ray photoelectron spectroscopy (VB-XPS) was employed to probe the relative positions of the valence band maximum (VBM) and Fermi level (E_F) in the three single-molecule GQDs.[35] As shown in Fig. 4H and S45, the energy difference between the valence band and Fermi level (E_v) was determined using the linear extrapolation method, yielding values of 3.30 eV (12Me-GQD), 3.77 eV (12Br-GQD), and 3.65 eV (6Br-6Me-GQD). The introduction of electron-withdrawing –Br groups significantly elevates E_v, as the –Br-induced charge redistribution effect shifts valence band electrons toward higher binding energies. This observation aligns with the downward shift of the HOMO level observed in UPS analyses, confirming the electronic modulation capability of edge functionalization in tailoring the energy landscape of GQDs.

HOMO and LUMO energy level modulation. UPS analysis of the three single-molecule GQDs (Fig. 5A–C) reveals significant electronic structure variations governed by edge functional groups. The HOMO levels of 12Me-GQD, 12Br-GQD, and 6Br-6Me-GQD were determined to be −5.57 eV, −10.26 eV, and −6.12 eV, respectively. Corresponding work functions (Φ) follow a similar trend: −1.81 eV (12Me-GQD), −6.36 eV (12Br-GQD), and −2.19 eV (6Br-6Me-GQD). Combined with UV-vis absorption data (Fig. S44), the LUMO levels were calculated to be −1.40 eV (12Me-GQD), −6.26 eV (12Br-GQD), and −1.94 eV (6Br-6Me-GQD). As summarized in Fig. 5D, edge substituents bidirectionally modulate energy levels: electron-withdrawing -Br groups substantially lower HOMO and LUMO levels *via* inductive and conjugative effects, while electron-donating $-CH_3$ groups elevate these levels through σ–π hyperconjugation.[36] The alternating $-Br/-CH_3$ arrangement in 6Br–6Me-GQD creates localized donor–acceptor microdomains, resulting in intermediate HOMO (−6.12 eV) and LUMO (−1.94 eV) levels between those of 12Me-GQD and 12Br-GQD. This demonstrates atomic-level precision in tuning electronic structures using only –Br and $-CH_3$ groups.

The consistency between UPS and VB-XPS data, where valence band-Fermi level gaps (E_v) align with HOMO level shifts, confirms the efficacy of edge functionalization in modulating GQD electronic configurations. Critically, the three GQDs share identical core dimensions and architectures, yet their electronic structures are precisely tailored by varying substituent type, electron-donating/withdrawing capacity, and spatial distribution (single kind of group substitution *vs.* alternating substitution). This approach enables size-independent bandgap and luminescence engineering, overcoming the limitations of conventional GQDs reliant on dimensional control.

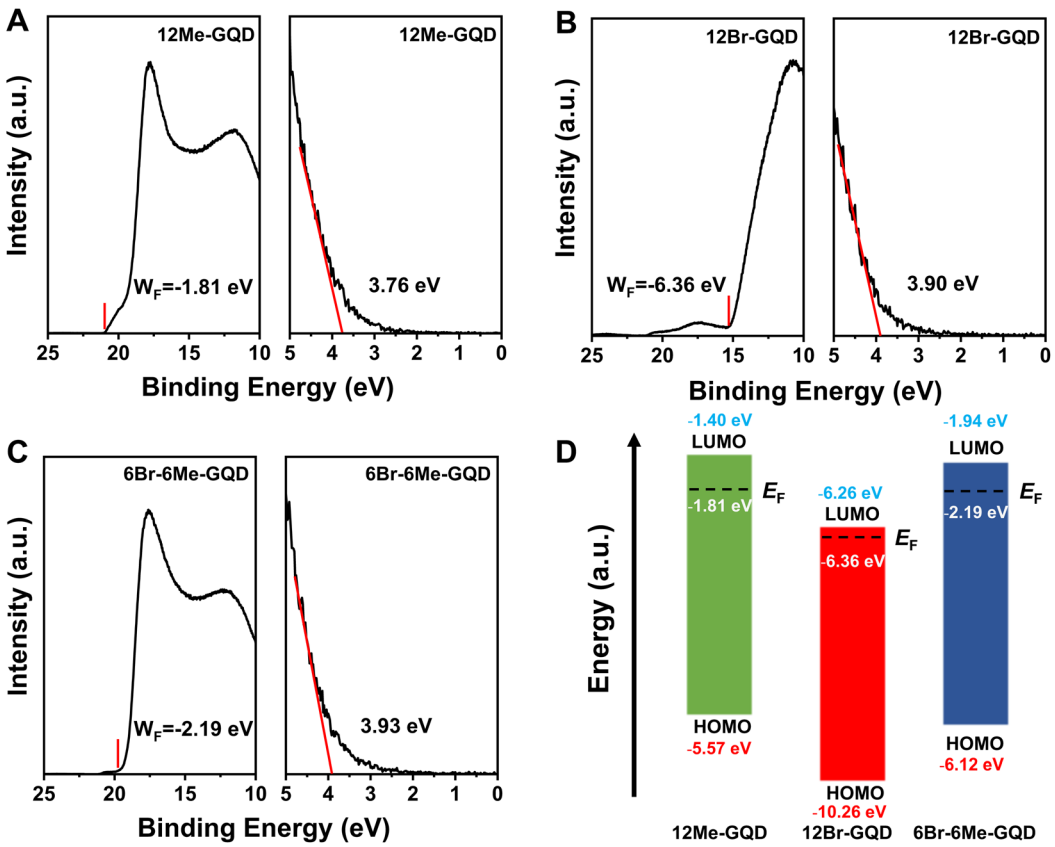

Fig. 5 (A) UPS spectra of near Fermi energy (low binding energy) and secondary electron cut-off (high binding energy) regions of 12Me-GQD; (B) UPS spectra of near Fermi energy (low binding energy) and secondary electron cut-off (high binding energy) regions of 12Br-GQD. (C) UPS spectra of near Fermi energy (low binding energy) and secondary electron cut-off (high binding energy) regions of 6Br-6Me-GQD. (D) Internal energy level changes in single-molecule GQDs due to modification of electron donor (Me) and electron acceptor (Br) molecules.

Structure–property relationship between the electronic structure and optical properties

The luminescence mechanism of GQDs remains a pivotal yet challenging research focus, as conventional synthesis methods yield heterogeneous mixtures that obscure precise structure–property correlations.[13] Addressing this bottleneck, this work develops an innovative modular organic synthesis strategy to prepare three monodisperse single-molecule GQDs with identical core structures and atomically controlled edge functionalities, enabling systematic investigation of surface-dependent luminescence mechanisms. As summarized in Table 1, comprehensive analyses of steady-state/time-resolved fluorescence spectra, UV-vis absorption profiles, and energy-level data reveal that edge functional group type and spatial distribution directly modulate electronic structures, thereby governing optical properties such as emission wavelength, fluorescence lifetime, and quantum yield (QY). Electron-withdrawing –Br substituents lower the LUMO level (12Br-GQD: $E_{LUMO} = -6.26$ eV), reducing the HOMO–LUMO gap ($E_g = 4.00$ eV) and red-shifting emission to 621 nm, while electron-donating $-CH_3$ groups elevate the HOMO level (12Me-GQD: $E_{HOMO} = -5.57$ eV) *via* σ–π hyperconjugation, expanding π-conjugation to increase E_g to 4.17 eV and blue-shift emission to 502 nm. The heavy-atom effect of -Br enhances intersystem crossing (ISC) to nonradiative triplet states, yielding the lowest QY for 12Br-GQD (4.22%), whereas $-CH_3$ suppresses nonradiative decay (k_{nr}), elevating 12Me-GQD's QY to 9.15%. The alternating –Br/$-CH_3$ configuration in 6Br–6Me-GQD introduces localized donor–acceptor microdomains, generating dual emission peaks and intermediate fluorescence lifetimes.

Energy-level engineering further demonstrates that –Br's strong electron-withdrawing capacity (Hammett constant $\sigma_p = +0.23$) lowers the HOMO level by 4.14 eV compared to that of 6Br-6Me-GQD, while σ–π hyperconjugation from $-CH_3$ (Hammett constant $\sigma_p = -0.17$) slightly elevates the LUMO level. By decoupling structural variables, this modular approach enables atomic-level tuning of HOMO/LUMO levels through inductive and conjugative effects, overcoming the size-dependent limitations of conventional GQDs. This paradigm advances the rational design of carbon-based quantum dots with tailored optoelectronic properties, offering transformative potential for single-molecule photonic devices and precision bioimaging probes.

Table 1 Parameters related to electronic structure–optical properties

	12Me-GQD	12Br-GQD	6Br-6Me-GQD
HOMO (eV)	−5.57	−10.26	−6.12
LUMO (eV)	−1.40	−6.26	−1.94
Φ (eV)	−1.81	−6.36	−2.19
E_V (eV)	3.30	3.77	3.65
E_g (eV)	4.17	4.00	4.18
$\lambda_{ex\ max}$ (nm)	502	621	409, 476
PL lifetime (ns)	9.26	4.10	3.62
PLQY (%)	9.15	4.22	5.53

ROS generation efficiency

Remarkably, the three single-molecule GQDs synthesized in this work exhibit robust photosensitizing properties under hypoxic conditions, generating substantial ROS upon visible light irradiation. Using the fluorescent probe DCFH to capture ROS, the ROS generation capabilities of these materials under hypoxia were investigated *via* fluorescence spectroscopy. As shown in Fig. 6A–C, ROS production was monitored under irradiation ($\lambda = 460$ nm, 20 mW cm^{-2}) at various time intervals. The data reveal that 12Me-GQD and 6Br-6Me-GQD efficiently release ROS under illumination, converting non-fluorescent DCFH into highly fluorescent DCF, as evidenced by a pronounced fluorescence enhancement. The fluorescence intensity exhibited a positive correlation with irradiation time, showing 2.1-fold and 3.8-fold increases after 10 min for 12Me-GQD and 6Br-6Me-GQD, respectively (Fig. 6A and C). In contrast, 12Br-GQD demonstrated no detectable ROS generation under identical conditions (Fig. 6B).

Fluorescence-based assessment demonstrates a strong correlation between the photodynamic activity of single-molecule GQDs and the electronic characteristics of their edge substituents. 12Br-GQD exhibits no ROS generation under illumination due to energy-level mismatch and triplet-state quenching effects. Concurrently, the heavy-atom effect of bromine promotes nonradiative vibrational relaxation of excited-state energy into heat rather than photosensitization. In contrast, electron-donating methyl ($-CH_3$) groups enhance ROS generation in 12Me-GQD, as evidenced by a 2.1-fold increase in probe fluorescence intensity. Notably, the 6D–π–6A-type GQD achieves a 3.8-fold fluorescence enhancement, representing a 1.8-fold improvement compared to the 12D–A-type GQD. This enhancement arises from alternating $-CH_3$ and –Br substituents, which create multiple intramolecular electron donor–acceptor microdomains, optimizing charge separation and interfacial electron transfer efficiency to facilitate directional migration of photogenerated electrons and holes. Critically, although bromine's heavy-atom effect enhances intersystem crossing, the alternating architecture of the 6D–π–6A-type GQD confines nonradiative quenching to localized regions, preserving overall ROS generation capacity. This unique property enables efficient ROS production even under hypoxic conditions, offering a novel strategy for photodynamic therapy in deep tumor tissues.

To further investigate the ROS generation mechanism, electron paramagnetic resonance (EPR) is adopted to detect the types of ROS that are generated by as-prepared single-molecule GQDs. As shown in Fig. 6D and F, the EPR data indicate that both 12Me-GQD and 6Br-6Me-GQD generate singlet oxygen ($^1O_2$) under light irradiation, confirmed by the distinct TEMP-$1O_2$ triplet signal, while as displayed in Fig. 6G and I, no Type I radicals (*e.g.*, ·OH and $O_2^{\cdot-}$) were detected by DMPO from them. For 12Br-GQD, noType I or Type II ROS were detected under light irradiation (Fig. 6E and H), which is consistent with its inert electronic structure. EPR data unambiguously prove that 12Me-GQD and 6Br-6Me-GQD operate *via* a Type II ($^1O_2$) photodynamic pathway under tested conditions. To investigate

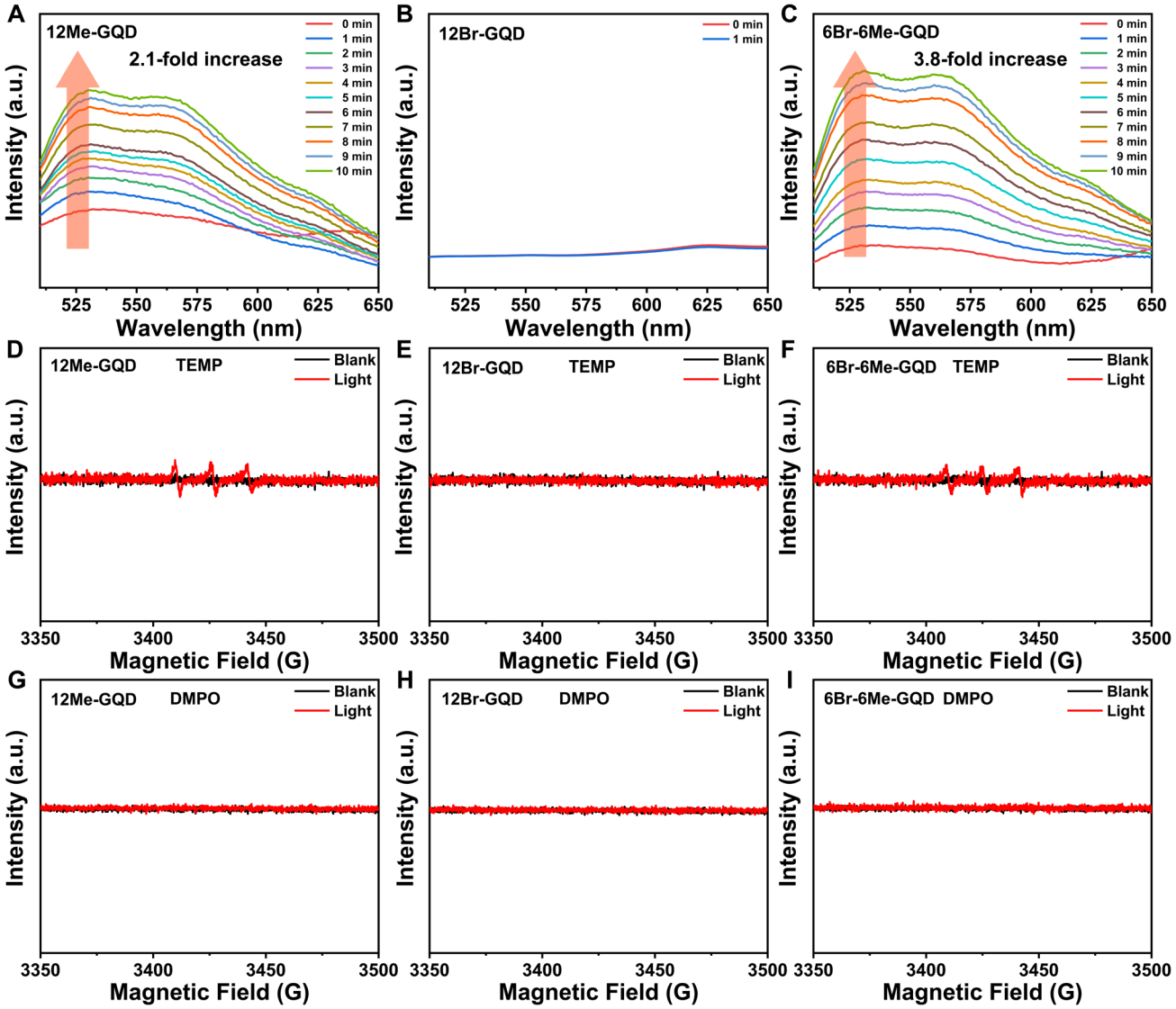

Fig. 6 ROS release ability of (A) 12Me-GQD, (B) 12Br-GQD and (C) 6Br-6Me-GQD (100 μmol L^{-1}, solvent: chloroform; $\lambda = 460$ nm, 20 mW cm^{-1-2}). (D–F) Detection of ROS based on electron paramagnetic resonance (EPR). Using TEMP as an indicator probe for singlet oxygen ($^1O_2$) generated by 12Me-GQD, 12Br-GQD and 6Br-6Me-GQD (100 μmol L^{-1}, xenon lamp (300 W) for 30 s). (G–I) Using DMPO as an indicator probe for ·OH generated by 12Me-GQD, 12Br-GQD and 6Br-6Me-GQD (100 μmol L^{-1}, xenon lamp (300 W) for 30 s).

the ROS generation capacity under hypoxic conditions, the $^1O_2$ quantum yields of 12Me-GQD and 6Br-6Me-GQD were determined using disodium 9,10-anthracenedipropionate (Na_2-ADPA) as a reference, yielding values of 0.48 and 0.68, respectively. This is consistent with the ROS generation capacity detected by DCFH, indicating that the 6D–π–6A type GQD exhibits significant ROS generation capability due to its multiple transport pathways (Fig. S46).

To verify the precise regulation of ROS generation by edge electronic structures, we performed theoretical calculations using Gaussian 16.[37,38] Considering the substantial computational complexity of full-sized single-molecule GQDs, we adopted scientifically validated fragment models (4Me-GQD, 4Br-GQD, and 2Br-2Me-GQD shown in Fig. S47), which retain the core electronic features and edge configuration characteristics of their parent systems. The π-conjugated cores of large GQDs exhibit size-invariant frontier orbital localization, while edge functional groups dominate electronic modulation—enabling one-third-sized fragments to reproduce the overall trends.

The fragment models accurately recapitulate the electronic regulation mechanisms of full-sized GQDs. Theoretical calculations reveal that the HOMO/LUMO shifting trends of the fragment models are consistent with those of full-sized GQDs (Fig. S48, Tables S8 and S9). Both theoretical calculations and experimental results confirm the following: electron-donating –CH_3 groups enhance carrier separation through localized positive electrostatic potential, maintaining ROS activity; electron-withdrawing -Br groups narrow the energy gap, causing fluorescence redshift, but trigger triplet state quenching to suppress ROS; the alternating arrangement of electron-

donating/withdrawing groups (6Br-6Me-GQD) constructs intramolecular multi-electron transport pathways, resulting in the highest ROS generation efficiency. The fragment models precisely validate the directional electronic modulation effects of the aforementioned groups, providing an atomic-level theoretical blueprint for the design of hypoxia-tolerant GQDs.

Atomic charge analysis provides a direct means to assess whether specific atoms and substituents are electron-donating or electron-withdrawing. We employed the standard Hirshfeld method to compute atomic and group charges (Fig. S47). In 4Me-GQD, all methyl groups carry positive charges, demonstrating that $-CH_3$ is electron-donating; while in 4Br-GQD, all bromine atoms bear negative charges, indicating that –Br is electron-withdrawing. Notably, in 2Br-2Me-GQD, the methyl groups at sites 2 and 3 exhibit greater positive charge relative to those in 4Me-GQD, implying enhanced electron donation, while the bromine atoms at sites 1 and 4 show more negative charge relative to 4Br-GQD, indicating increased electron withdrawal. These results suggest that, in 2Br-2Me-GQD, the bromine atoms withdraw more electrons, predominantly supplied by the methyl groups.

Since the molecular electrostatic potential (ESP) is closely related to charge distribution in chemical systems, we plot the mapping ESP onto the molecular van der Waals (vdW) surface as an isosurface of electron density of 0.001 a.u. (Fig. S49).[39,40] The results show that for 4Me-GQD, methyl groups (Me) exhibit positive ESP (electron-donating), while the conjugated core shows negative ESP (electron-withdrawing); for 4Br-GQD, bromine atoms (Br) exhibit negative ESP (electron-withdrawing), and the bay regions show positive ESP (electron-deficient); for 2Br-2Me-GQD, the spatial separation of Br (negative ESP) and Me (positive ESP) further forms dipoles, enhancing charge separation efficiency. The simulated ESP distribution patterns, which identify electron-rich/electron-deficient regions, are consistent with the theoretical design concepts. This approach provides atomic-level insights into our understanding of electronic structure control strategies, confirming that functional group engineering can directly modulate the energy band structure, thereby enhancing photodynamic efficacy.

Through comprehensive analysis of the structures and properties of three single-molecule GQDs, it is clear that the electronic structure significantly influences their luminescence properties and photo-induced ROS generation capability, serving as a critical factor determining the performance of carbon nanomaterials. As shown in Fig. 7, the three single-molecule GQDs share identical core structures but differ in surface functional group types and quantities, exhibiting three distinct electronic configurations: 12D–A, D–12A, and 6D–π–6A. These configurations demonstrate green, red, and blue emission, respectively, collectively spanning the entire visible spectrum. Notably, the 12D–A configuration achieves the highest photoluminescence quantum yield while D–12A shows the lowest. Under hypoxic conditions, both 12D–A and 6D–π–6A GQDs generate substantial ROS upon illumination, whereas D–12A GQDs exhibit negligible ROS production. These findings highlight that precise modulation of electronic structures can effectively optimize the imaging capabilities and therapeutic efficacy of carbon nanomaterials, particularly enabling targeted applications in tumor systems with hypoxic microenvironments. This positions single-molecule GQDs as promising nanomedicine candidates for advanced antitumor therapies.

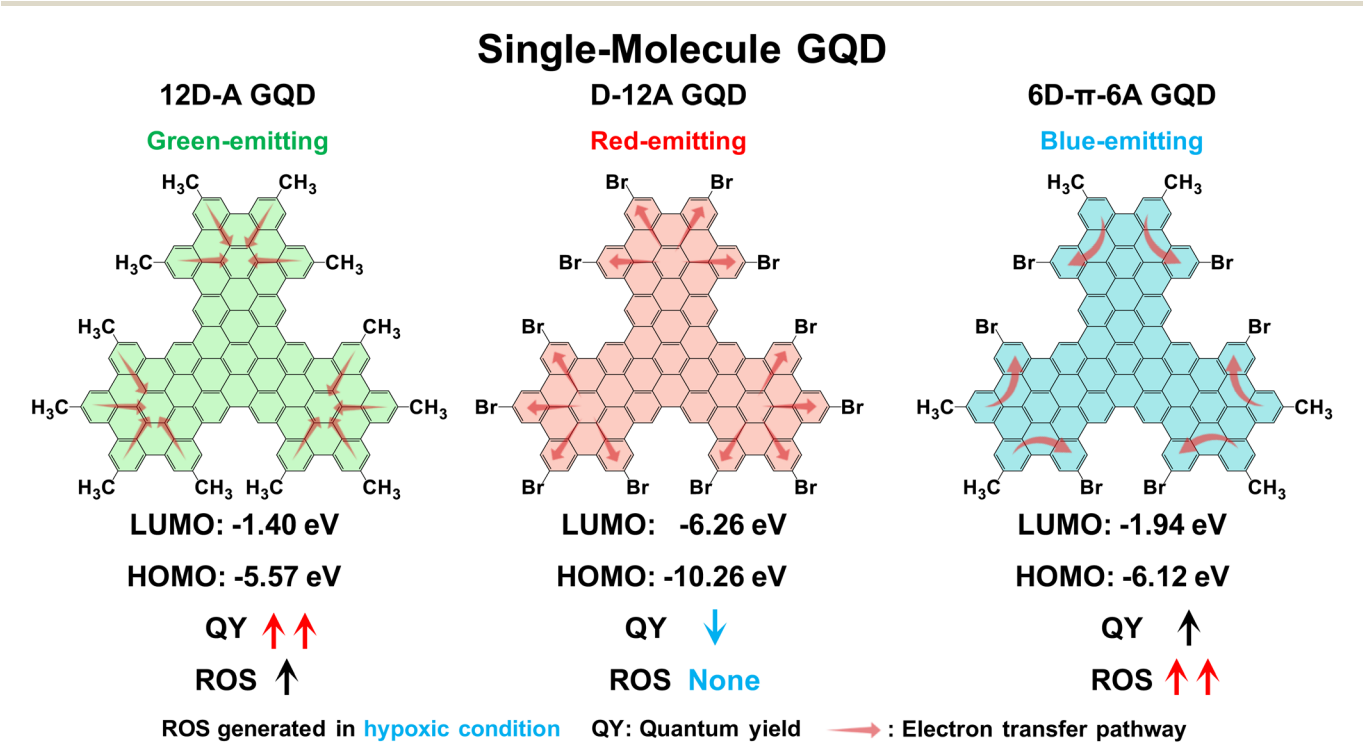

Fig. 7 Mechanism diagram of the structure–property relationship of single-molecule GQDs.

Conclusions

This work develops a modular organic synthesis strategy to efficiently prepare three single-molecule GQDs with identical core structures and precisely controlled edge functional groups (12Me-GQD, 12Br-GQD, and 6Br-6Me-GQD), achieving atomic-level controllable synthesis and electronic structure modulation of GQDs. These single-molecule GQDs are respectively functionalized with 12 $-CH_3$ groups, 12-Br groups, and 6 alternating $-CH_3$/–Br groups at their peripheries. The distinct electronic characteristics and spatial arrangements of electron-donating ($-CH_3$) and electron-withdrawing (–Br) groups profoundly influence the materials' electronic structures. The effects of the electronic structures on energy levels, luminescent properties, and light-induced ROS generation efficiency were systematically investigated, with fundamental structure–property and structure–activity relationships elucidated. It was revealed that electron-donating $-CH_3$ groups elevated both HOMO and LUMO energy levels through σ–π hyperconjugation effects, resulting in an expanded bandgap. This led to blue-shifted fluorescence emission and enhanced fluorescence quantum yield. Additionally, photoinduced carrier separation efficiency was significantly improved by $-CH_3$ groups, enabling 12Me-GQD to exhibit superior photodynamic ROS generation capability. In contrast, electron-withdrawing –Br groups reduced molecular orbital energy levels through inductive and conjugative effects, narrowing the bandgap and inducing red-shifted emission with diminished quantum yield. Due to energy-level mismatch and triplet-state quenching effects, ROS generation was completely suppressed in 12Br-GQD under illumination. The alternating donor–acceptor architecture of 6Br-6Me-GQD was demonstrated to exhibit dual emission peaks and multiple electron transfer microdomains, which synergistically enhanced carrier separation efficiency and achieved optimal ROS generation performance. Conventional GQD modifications typically rely on size-dependent bandgap tuning through core conjugation area adjustment. In this work, identical core structures were maintained while luminescence properties were precisely regulated through edge functionalization. HOMO/LUMO levels and bandgaps were modulated by engineering the electronic nature (donor/acceptor) and spatial arrangement (single kind of group substitution/alternating substitution) of peripheral groups. This approach established a novel edge-state modulation paradigm, advancing the mechanistic understanding of molecular nanomaterial engineering beyond traditional size-dependent strategies.

Furthermore, the single-molecule GQDs synthesized in this work exhibit highly efficient light-triggered ROS generation under hypoxic conditions, demonstrating exceptional compatibility with oxygen-deficient tumor microenvironments. Distinct from conventional photosensitizers (*e.g.*, porphyrins) that require high oxygen concentrations, these structurally well-defined nanomaterials possess unambiguous molecular architectures and precise molecular weights, overcoming the intrinsic heterogeneity limitations of traditional nanomaterials. This advancement addresses the critical challenge of treating deep-seated tumor tissues, positioning this series of single-molecule GQDs as promising candidates for next-generation nanomedicines. By employing the modular organic synthesis strategy for single-molecule GQDs, precise control over both the microstructure and electronic configuration of the materials was achieved. This methodology enabled the systematic elucidation of structure–property relationships governing luminescent characteristics and structure–activity relationships dictating photodynamic efficacy. A comprehensive investigation spanning the entire development chain, from controlled synthesis to detailed characterization and functional application, was conducted. This work establishes a robust foundation for the precise engineering and structural innovation of nanocarbon materials, advancing the frontier of molecular-level design and application in nanomedicine.

Author contributions

J. C. and T. G. designed the study and developed the theoretical framework. J. C., B. L., D. L., and S. Y. performed chemical synthesis and conducted molecular characterization. J. C., B. L. and T. G. conducted the investigation on the structure–activity relationship. T. G. and J. C. carried out data curation, formal analysis, and visualization, and drafted the manuscript. T. G. acquired research funding, provided methodological guidance, supervised the research, and contributed critical resources. J. Q. conducted the theoretical calculation experiments. Z. L. and Y. L. provided technical expertise and offered conceptual advice. T. G. and Y. L. jointly administered the project, validated experimental results, and revised the manuscript. All authors engaged in data interpretation, provided substantive feedback during manuscript preparation, and approved the final version for publication.

Conflicts of interest

The authors declare no competing financial interest.

Data availability

The data supporting this article have been included as part of the SI.

Supplementary information: The general information, methods, NMR spectra, synthetic details, and supplementary discussions associated with this article. See DOI: **https://doi.org/10.1039/d5sc03593g**.

Acknowledgements

This research was financially supported by funds from the National Natural Science Foundation of China (22403072), the Department of Education of Hubei Province of China (Q20231103 and B2021014), the Natural Science Foundation of Hubei Province (2025AFA009), the Chutian Scholar Program of Hubei Province of China (2021), the Key Laboratory of Hubei Province for Coal Conversion and New Carbon Materials (Wuhan University of Science and Technology) (WKDM202110),

and the Scientific Research Foundation (Wuhan University of Science and Technology) (1050029). The authors are thankful for the support from the Analytical & Testing Center at Wuhan University of Science and Technology.

Notes and references

1 A. Sharma, P. Verwilst, M. Li, D. Ma, N. Singh, J. Yoo, Y. Kim, Y. Yang, J.-H. Zhu, H. Huang, X.-L. Hu, X.-P. He, L. Zeng, T. D. James, X. Peng, J. L. Sessler and J. S. Kim, Theranostic Fluorescent Probes, *Chem. Rev.*, 2024, **124**, 2699–2804.

2 J. Shin, N. Kang, B. Kim, H. Hong, L. Yu, J. Kim, H. Kang and J. S. Kim, One-dimensional nanomaterials for cancer therapy and diagnosis, *Chem. Soc. Rev.*, 2023, **52**, 4488–4514.

3 S. Chung, R. A. Revia and M. Zhang, Graphene Quantum Dots and Their Applications in Bioimaging, Biosensing, and Therapy, *Adv. Mater.*, 2021, **33**, e1904362.

4 H. Yan, Q. Wang, J. Wang, W. Shang, Z. Xiong, L. Zhao, X. Sun, J. Tian, F. Kang and S. H. Yun, Planted Graphene Quantum Dots for Targeted, Enhanced Tumor Imaging and Long-Term Visualization of Local Pharmacokinetics, *Adv. Mater.*, 2023, **35**, 2210809.

5 M. Hassnain, L. S. van Hofwegen, H. N. Kaleli, T. Kubanaliev, Z. Eroglu, A. Onal, P. P. S. Balraadjsing, O. Metin, F. Alkan, S. A. J. Zaat and S. Nizamoglu, Ultra-Effective Light-Activated Antibacterial Activity via Carboxyl Functionalized Graphene Quantum Dots and Films, *Adv. Funct. Mater.*, 2025, 2421537, DOI: **10.1002/adfm.202421537**.

6 W.-S. Kuo, C.-Y. Chang, H.-Y. Chuang, P.-L. Su, J.-Y. Wang, P.-C. Wu, H.-F. Kao, S.-W. Tseng, S.-H. Lin, Y.-S. Lin and C.-C. Chang, Single-sized N-functionality graphene quantum dot in tunable dual-modality near infrared-I/II illumination detection and photodynamic therapy under multiphoton nonlinear excitation, *Biosens. Bioelectron.*, 2023, **241**, 115648.

7 L. L. Shi, B. Y. Wang and S. Y. Lu, Efficient bottom-up synthesis of graphene quantum dots at an atomically precise level, *Matter*, 2023, **6**, 728–760.

8 Y. Yan, J. Gong, J. Chen, Z. Zeng, W. Huang, K. Pu, J. Liu and P. Chen, Recent Advances on Graphene Quantum Dots: From Chemistry and Physics to Applications, *Adv. Mater.*, 2019, **31**, e1808283.

9 R. Wang, M. He, Z. Zhang, T. Qiu, Y. Xi, X. Zeng, J. Fan, W. Sun and X. Peng, Photodynamic therapy promotes hypoxia-activated nitrogen mustard drug release, *Smart Mol.*, 2024, **2**, e20240010.

10 C. Zhao, C. Qu, Y. Hu, F. Wu, S. Liu, F. Cai, Y. Chen, Y. Qiu and Z. Shen, Orbicular-Donor-Acceptor System in N-doped Nanographene for Highly Efficient NIR-II Photothermal Therapy, *Adv. Healthcare Mater.*, 2024, **13**, 2402545.

11 H. He, J. Lee, Z. Zong, N. Liu, Y. Noh, V. M. Lynch, J. Oh, J. Kim, J. L. Sessler and X. S. Ke, Precisely metal doped nanographenes via a carbaporphyrin approach, *Nat. Commun.*, 2025, **16**, 1534.

12 J. Chen, S. Yin, f. Yang, S. Guo, J. Zhang, Z. Lu and T. Gao, A Single-Molecule Graphene Quantum Dot: a Novel Efficient Photosensitizer for Photodynamic Cancer Therapy, *Chem. Sci.*, 2025, **16**, 13923–13934.

13 M. Jiang, Y. Sun, M. Chen, H. Ji, Y. Liu, R. Qin, X. Li, H. Gao, R. Zhang and L. Zhang, Multicolor luminescence of carbon Dots: From mechanisms to applications, *Chem. Eng. J.*, 2024, **496**, 153761.

14 M. Cao, X. Zhao and X. Gong, Ionic Liquid-Assisted Fast Synthesis of Carbon Dots with Strong Fluorescence and Their Tunable Multicolor Emission, *Small*, 2022, **18**, 2106683.

15 M. A. Sk, A. Ananthanarayanan, L. Huang, K. H. Lim and P. Chen, Revealing the tunable photoluminescence properties of graphene quantum dots, *J. Mater. Chem. C*, 2014, **2**, 6954–6960, DOI: **10.1039/C4TC01191K**.

16 Y. Dang, Y. Liu, P. Xiang, Z. Tan, Z. Tian, M. Greiner, S. Heumann, Y. Ding and Z. A. Qiao, Carbon Surface Chemistry: Benchmark for the Analysis of Oxygen Functionalities on Carbon Materials, *Adv. Mater.*, 2025, 2418239, DOI: **10.1002/adma.202418239**.

17 J. Ge, M. Lan, B. Zhou, W. Liu, L. Guo, H. Wang, Q. Jia, G. Niu, X. Huang, H. Zhou, X. Meng, P. Wang, C.-S. Lee, W. Zhang and X. Han, A graphene quantum dot photodynamic therapy agent with high singlet oxygen generation, *Nat. Commun.*, 2014, **5**, 4596.

18 X.-H. Ma, X. Gao, J.-Y. Chen, M. Cao, Q. Dai, Z.-K. Jia, Y.-B. Zhou, X.-J. Zhao, C. Chu, G. Liu and Y.-Z. Tan, Soluble Nanographene C222: Synthesis and Applications for Synergistic Photodynamic/Photothermal Therapy, *J. Am. Chem. Soc.*, 2024, **146**, 2411–2418.

19 Y. Yang, B. Wang, X. Zhang, H. Li, S. Yue, Y. Zhang, Y. Yang, M. Liu, C. Ye, P. Huang and X. Zhou, Activatable Graphene Quantum-Dot-Based Nanotransformers for Long-Period Tumor Imaging and Repeated Photodynamic Therapy, *Adv. Mater.*, 2023, **35**, 2211337.

20 Y. Yue, B. Li, D. Wang, C. Wu, Z. Li and B. Liu, Optimizing Photosensitizers with Type I and Type II ROS Generation Through Modulating Triplet Lifetime and Intersystem Crossing Efficiency, *Adv. Funct. Mater.*, 2024, **35**, 2414542.

21 J. Gao, H. Yang, Y. Lu, Q. Shi, S. Xu, W. Wu, F. Hu and B. Liu, Anthracene-Bridged Photosensitizers for Effective and Safe Photodynamic Therapy, *Chem. Mater.*, 2023, **35**, 1229–1237.

22 X. Li, L. Huang, G. Baryshnikov, A. Ali, P. Dai, Z. Yang, Y. Sun, C. Dai, Z. Guo, Q. Zhao, F. Zhang and L. Zhu, Thermally Activated Delayed Fluorescence-Guided Photodynamic Therapy Through Skeleton-Homologous Nanoparticles: a Rational Material Design for High-Efficient and High-Contrast Theranostics, *Adv. Mater.*, 2025, **37**, 2500236.

23 N. Iwashita, C. R. Park, H. Fujimoto, M. Shiraishi and M. Inagaki, Specification for a standard procedure of X-ray diffraction measurements on carbon materials, *Carbon*, 2004, **42**, 701–714.

24 A. C. Ferrari, J. C. Meyer, V. Scardaci, C. Casiraghi, M. Lazzeri, F. Mauri, S. Piscanec, D. Jiang, K. S. Novoselov, S. Roth and A. K. Geim, Raman Spectrum of Graphene and Graphene Layers, *Phys. Rev. Lett.*, 2006, **97**, 187401.

25 J.-B. Wu, M.-L. Lin, X. Cong, H.-N. Liu and P.-H. Tan, Raman spectroscopy of graphene-based materials and its applications in related devices, *Chem. Soc. Rev.*, 2018, **47**, 1822–1873.

26 H. J. Yen, H. Tsai, M. Zhou, E. F. Holby, S. Choudhury, A. Chen, L. Adamska, S. Tretiak, T. Sanchez, S. Iyer, H. Zhang, L. Zhu, H. Lin, L. Dai, G. Wu and H. L. Wang, Structurally Defined 3D Nanographene Assemblies via Bottom-Up Chemical Synthesis for Highly Efficient Lithium Storage, *Adv. Mater.*, 2016, **28**, 10250–10256.

27 M. Sarker, C. Dobner, P. Zahl, C. Fiankor, J. Zhang, A. Saxena, N. Aluru, A. Enders and A. Sinitskii, Porous Nanographenes, Graphene Nanoribbons, and Nanoporous Graphene Selectively Synthesized from the Same Molecular Precursor, *J. Am. Chem. Soc.*, 2024, **146**, 14453–14467.

28 F. Baskoro, H. Q. Wong, S. Najman, P.-Y. Yang, J. J. H. Togonon, Y.-C. Ho, M.-C. Tseng, D.-L. M. Tzou, Y.-R. Kung, C.-W. Pao and H.-J. Yen, Lithium-Ion Dynamic and Storage of Atomically Precise Halogenated Nanographene Assemblies via Bottom-Up Chemical Synthesis, *ACS Appl. Mater. Interfaces*, 2024, **16**, 29016–29028.

29 T. Gao, X. Wang, J. Zhao, P. Jiang, F. L. Jiang and Y. Liu, Bridge between Temperature and Light: Bottom-Up Synthetic Route to Structure-Defined Graphene Quantum Dots as a Temperature Probe In Vitro and in Cells, *ACS Appl. Mater. Interfaces*, 2020, **12**, 22002–22011.

30 T. Gao, X. Wang, L. Y. Yang, H. He, X. X. Ba, J. Zhao, F. L. Jiang and Y. Liu, Red, Yellow, and Blue Luminescence by Graphene Quantum Dots: Syntheses, Mechanism, and Cellular Imaging, *ACS Appl. Mater. Interfaces*, 2017, **9**, 24846–24856.

31 K. Jiang, S. Hu, Y. Wang, Z. Li and H. Lin, Photo-Stimulated Polychromatic Room Temperature Phosphorescence of Carbon Dots, *Small*, 2020, **16**, 2001909.

32 Y. Zhang and S. Lu, Lasing of carbon dots: Chemical design, mechanisms, and bright future, *Chem*, 2024, **10**, 134–171.

33 F. F. Wang, Y. X. Wang, Q. Wu, L. Chai, X. W. Chen and Y. Z. Tan, Nanographene with a Nitrogen-Doped Cavity, *Angew. Chem., Int. Ed.*, 2023, **63**, e202315302.

34 H. Wang, X. C. Liu, X. Y. Yan, J. W. Fan, D. W. Li, J. S. Ren and X. G. Qu, A MXene-derived redox homeostasis regulator perturbs the Nrf2 antioxidant program for reinforced sonodynamic therapy, *Chem. Sci.*, 2022, **13**, 6704–6714.

35 P. Han, I. C. Hou, H. Lu, X. Y. Wang, K. Müllen, M. Bonn, A. Narita and E. Canovas, Chemisorption of Atomically Precise 42-Carbon Graphene Quantum Dots on Metal Oxide Films Greatly Accelerates Interfacial Electron Transfer, *J. Phys. Chem. Lett.*, 2019, **10**, 1431–1436.

36 Q. Zhang, R. Y. Wang, B. W. Feng, X. X. Zhong and K. Ostrikov, Photoluminescence mechanism of carbon dots: triggering high-color-purity red fluorescence emission through edge amino protonation, *Nat. Commun.*, 2021, **12**, 6856.

37 M. J. Frisch, G. W. Trucks, H. B. Schlegel, G. E. Scuseria, M. A. Robb, J. R. Cheeseman, G. Scalmani, V. Barone, G. A. Petersson, H. Nakatsuji, X. Li, M. Caricato, A. V. Marenich, J. Bloino, B. G. Janesko, R. Gomperts, B. Mennucci, H. P. Hratchian, J. V. Ortiz, A. F. Izmaylov, J. L. Sonnenberg, Williams, F. Ding, F. Lipparini, F. Egidi, J. Goings, B. Peng, A. Petrone, T. Henderson, D. Ranasinghe, V. G. Zakrzewski, J. Gao, N. Rega, G. Zheng, W. Liang, M. Hada, M. Ehara, K. Toyota, R. Fukuda, J. Hasegawa, M. Ishida, T. Nakajima, Y. Honda, O. Kitao, H. Nakai, T. Vreven, K. Throssell, J. A. Montgomery Jr, J. E. Peralta, F. Ogliaro, M. J. Bearpark, J. J. Heyd, E. N. Brothers, K. N. Kudin, V. N. Staroverov, T. A. Keith, R. Kobayashi, J. Normand, K. Raghavachari, A. P. Rendell, J. C. Burant, S. S. Iyengar, J. Tomasi, M. Cossi, J. M. Millam, M. Klene, C. Adamo, R. Cammi, J. W. Ochterski, R. L. Martin, K. Morokuma, O. Farkas, J. B. Foresman and D. J. Fox, *Gaussian 16 Revision C.02*, 2019.

38 W. Humphrey, A. Dalke and K. Schulten, *J. Mol. Graphics*, 1996, **14**, 33–38.

39 J. Zhang and T. Lu, Efficient evaluation of electrostatic potential with computerized optimized code, *Phys. Chem. Chem. Phys.*, 2021, **23**, 20323–20328.

40 T. Lu and F. Chen, Multiwfn: A multifunctional wavefunction analyzer, *J. Comput. Chem.*, 2011, **33**, 580–592.